*Conference on Modelling Fluid Flow (CMFF'25)*
*The 19th International Conference on Fluid Flow Technologies*
*Budapest, Hungary, August 26 - August 29, 2025*

# MULTIPHASE MODEL OF THE MELT BLOWING PROCESS IN MULTI-HOLE NOZZLES

Fabian LEMARCHAND[1], Alejandro RIVAS[2], Alaine SALTERAIN[3]

[1] Department of Mechanical Engineering and Materials, TECNUN Escuela de Ingeniería, Universidad de Navarra, Paseo Manuel de Lardizabal, 13, San Sebastian E-20018, Spain. Tel.: +33 6 23 83 43 66, E-mail: flemarchand@unav.es
[2] Department of Mechanical Engineering and Materials, TECNUN Escuela de Ingeniería, Universidad de Navarra, Paseo Manuel de Lardizabal, 13, San Sebastian E-20018, Spain. E-mail: arivas@tecnun.es
[3] Valco Melton, Pol. Industrial Agustinos, Calle G, 34, Orcoyen 31160, Spain. E-mail: alaine.salterain@velcomelton.es

## ABSTRACT

Melt blowing is an industrial process used to design various products across different fields like surgical masks, filtration devices, diapers or electronic devices. The process consists in attenuating a fibre of adhesive using gases at a high velocity. Achieving optimal fibre attenuation is of paramount importance to get a convenient industrial application that meets quality requirements. The dynamics of this process is investigated by implementing a multiphase mathematical model that employs the Volume of Fluid (VOF) method. Three-dimensional multiphase simulations are conducted to gain insights into the influence of operating parameters on the fibre dynamics and attenuation. The simulation replicates the interaction between compressible air and the fluid fibre, which is treated as a non-Newtonian fluid with a temperature-dependent viscosity following a Cross-Arrhenius law. Attenuation results are compared with experimental measures and observations. By conducting multiphase simulations leveraging the capabilities of the VOF model, valuable insights into the dynamics and the physical properties of the fibres is obtained, contributing to the optimization of the melt blowing process in various industrial applications.

**Keywords : Melt blowing, Volume of Fluid (VOF), Non-Newtonian fluids, Computational Fluid Dynamics (CFD), Holt-melt adhesive, Turbulence damping**

## NOMENCLATURE

| | | |
|---|---|---|
| $A$ | $[m^{-1}]$ | interfacial area density |
| $B$ | [-] | turbulence damping factor |
| $c_p$ | $[J.kg^{-1}.K^{-1}]$ | specific heat at a constant pressure |
| $c_v$ | $[J.kg^{-1}.K^{-1}]$ | specific heat at a constant volume |
| $D$ | $[m]$ | fibre diameter |
| $D_0$ | $[m]$ | fibre diameter at the first measurement point (i.e. $Z$ = 0.53 $mm$) |
| $\underline{dr}$ | $[m]$ | cell to face distance vector |
| $E_a$ | $[J/mol]$ | activation energy of the fluid |
| $F_{CSF}$ | $[N/m^3]$ | surface tension force |
| $\underline{g}$ | $[m.s^{-2}]$ | gravitational acceleration vector |
| $k$ | $[J/kg]$ | turbulent kinetic energy |
| $l$ | $[m]$ | turbulent length scale |
| $M_f$ | $[kg]$ | mass of fibre present in the domain |
| $\dot{m}$ | $[kg/s]$ | mass flow rate |
| $m'$ | [-] | dimensionless flow rate ratio |
| $\underline{n}$ | [-] | surface normal vector |
| $N$ | [-] | power-law index |
| $p$ | $[Pa]$ | pressure field |
| $R$ | $[J.K^{-1}.mol^{-1}]$ | gas constant |
| $S_{\omega,i}$ | $[m^2/s^4]$ | turbulence damping source term |
| $t$ | $[s]$ | flow time |
| $T$ | $[K]$ | temperature field |
| $T_R$ | $[K]$ | Cross-Arrhenius model reference temperature |
| $T'$ | [-] | dimensionless temperature ratio |
| $\underline{u}$ | $[m/s]$ | velocity vector |
| $\alpha$ | [-] | volume fraction |
| $\beta$ | [-] | turbulence damping destruction term |
| $\dot{\gamma}$ | $[s^{-1}]$ | shear rate |
| $\delta_s$ | [-] | dirac distribution concentrated at the interface |
| $\Delta n$ | $[m]$ | grid size |
| $\Delta t$ | $[s]$ | time step size |
| $\vartheta$ | [-] | slope limiter value |
| $\kappa$ | $[W.m^{-1}.K^{-1}]$ | thermal conductivity |
| $\lambda$ | $[s]$ | Cross-law relaxation time |
| $\mu$ | $[Pa.s]$ | dynamic viscosity |
| $\mu_0$ | $[Pa.s]$ | zero-shear viscosity |
| $\mu_t$ | $[Pa.s]$ | turbulent viscosity |
| $\rho$ | $[kg/m^3]$ | density |
| $\sigma$ | $[N/m]$ | surface tension coefficient |
| $\varphi$ | [-] | flow variable |

| | | |
|---|---|---|
| $\bar{\varphi}$ | [-] | flow variable mean value |
| $\varphi'$ | [-] | flow variable fluctuating part |
| $\chi$ | $[m^{-1}]$ | local curvature at the interface |
| $\omega$ | $[m^2/s^3]$ | turbulent specific rate dissipation |

**Subscripts and Superscripts**

| | |
|---|---|
| $a$ | air phase |
| $amb$ | ambient |
| $Coarse$ | Coarsest grid |
| $f$ | fibre fluid phase |
| $face$ | grid face |
| $Fine$ | Finest grid |
| $i$ | $i$ phase |
| $Medium$ | Medium grid |
| $min$ | minimum value |
| $t$ | turbulent |
| $Z = Z_k$ | $Z_k = (7\ mm, 12\ mm)$ |

## 1. INTRODUCTION

The melt blowing process involves the extrusion of a polymer called fibre through a nozzle, where convergent air jets attenuate the polymer to create non-woven textiles with reduced adhesive usage. This process has been widely studied since its creation in the 1950s [1] to enhance its efficiency, improve product quality, and reduce energy consumption. This industrial process enables the production of high-filtration devices [2], that can be masks, diapers or disposable hygiene products in general. One of the main issues encountered in the melt-blowing process is the lack of reproducibility, by not being able to fully control the fibre pattern uniformity along the process. Defects like undesired breakups, shot formation and fibre vibrations tend to affect the fibre pattern, potentially leading to imperfections in the final application or altering the filtration functionalities of the product.

Although experimental setups composed of high-speed cameras, halogen lamps and diffuser glasses can capture all these phenomena [3], measuring the diameters and temperatures of the fibres is a challenging and costly process. Therefore, numerical methods techniques need to be explored to set up the process without having to perform these experiments. Computational fluid dynamics (CFD) simulations have been performed to study the airflow in the melt blowing process, focusing on different nozzle geometries and employing three-dimensional turbulent steady-state analyses. Single phase models of the airflow have been implemented to study the impact of different nozzle configurations on turbulence levels and air recirculation, two phenomena that might lead to the splitting of the fibre flow [4] [5]. Nonetheless, such models do not consider the presence of the fibre. A solution is to couple a one-dimensional model of the fibre flow with the airflow. This is done by incorporating drag and heat transfer exchange source terms to the momentum and heat transfer equations of the fibre flow using the fundamental equations of the melt-spinning process [6]. The source term coefficients might need adjustments to validate the melt-blowing process experimental results [7] [8] [9]. Nevertheless, these models do not take into account the fibre motion and its implications on the surrounding airflow. Multiphase models can be contemplated as an alternative to capture the complex physical coupling between the air and the fibre [10]. The computational resources required and the challenges associated with an accurate modelling of the multiphase nature of the process should be considered though, as the fluid properties are complex and the need for adequate spatial and temporal discretisation can result in significant time restrictions [11]. One of the most known models used in gas-liquid simulations is the Euler-Euler model, in applications that involve atomisation in particular. In such model, both phases are treated as interpenetrating continuum. This is particularly useful when breakups and bubble formation are expected, as in spray modelling [12], [13]. A similar approach has been employed to model the interaction between a gas and solid particles [14], [15], [16]. Other approaches combine the Euler-Euler model with the VOF model, the latter being primarily used to track the interface between two immiscible phases. Such hybrid methodology consists in using the Euler-Euler model to capture dispersed flow phenomena while the VOF model is used to model the internal gas-liquid flow [17], [18].
Nonetheless, implementing the VOF model without coupling it with the Euler-Euler model proved to be sufficient for investigating jet-instability and droplet formation in atomisation[19].

The model presented in this study employs the VOF model to track the interaction between the fibre and the airflow in a multi-hole nozzle structure used in the melt-blowing process. Such methodology has already been employed in swirl die structures [20]. Valuable information can be obtained on the flow thermophysical properties, the fibre dynamics and the fibre pattern by simulating under various operating conditions without having to conduct challenging and expensive experiments. The present work shows how CFD can be used as a decision support tool to optimise the configuration of complex manufacturing processes. Two different cases are compared to investigate the influence of the air-polymer flow rate on fibre pattern and fibre dynamics. The fibre attenuation and motion frequencies are analysed and compared with experimental results.

## 2. GOVERNING EQUATIONS

The VOF model is employed to track the interface between two immiscible fluids here, which are the air, modelled as an ideal gas and the polymer fibre fluid. The volume fraction $\alpha$ is calculated in a control volume to determine the presence of the primary (air) and secondary (polymer fibre fluid)

phases. When α=1, the control volume is full of adhesive, while when α=0, the control volume is full of air. The VOF model is governed by a set of equations that include the mass, momentum and energy conservation and the transport of the volume fraction:

$$\frac{\partial \rho}{\partial t} + div\,(\rho \underline{u}) = 0 \tag{1}$$

$$\frac{D(\rho \underline{u})}{Dt} = -\nabla p + div\left(\mu \nabla \underline{u} + \mu\left(\nabla \underline{u}\right)^T\right) + \sigma \chi \delta_s \underline{n} + \rho \underline{g} \tag{2}$$

$$\frac{D(\rho T)}{Dt} - div(\kappa \nabla T) + div\left(\underline{u} p\right) + \frac{D\left(\rho\left(0.5|\underline{u}|^2\right)\right)}{Dt}\left(\frac{\alpha}{c_{v,f}} + \frac{1-\alpha}{c_{v,a}}\right) = 0 \tag{3}$$

$$\frac{D(\rho \alpha)}{Dt} = 0 \tag{4}$$

$$\rho = \alpha \rho_f + (1-\alpha)\rho_a \tag{5}$$

$$\mu = \alpha \mu_f + (1-\alpha)\mu_a \tag{6}$$

$$\kappa = \alpha \kappa_f + (1-\alpha)\kappa_a \tag{7}$$

with $\underline{u}$ being the velocity vector, $\chi$ the local curvature at the interface, $\delta_s$ the dirac distribution concentrated on the interface, $\sigma$ the surface tension coefficient, $\rho_f$ the fibre fluid density, $\rho_a$ the air density, $\mu_f$ the fibre fluid viscosity, $\mu_a$ the air viscosity, $c_{v,f}$ the fibre fluid specific heat, $c_{v,a}$ the air specific heat, $\kappa_f$ the fibre fluid conductivity and $\kappa_a$ the air conductivity. $\underline{n}$ represents the surface normal. Its expression is $\underline{n} = \nabla \alpha$. Capillary effects are taken into account in this study. The Continuum Surface Force (CSF) model [21] is used to model the surface tension effect between the air and adhesive phases. A constant surface tension coefficient value of $\sigma = 0.03\ N/m$ is used in this study. The surface tension force $F_{CSF}$ is calculated using the following formulation:

$$F_{CSF} = \sigma \chi \nabla \alpha \tag{8}$$

where $\sigma$ is the surface tension coefficient, and $\nabla \alpha$ denotes the gradient of the volume fraction ($\alpha$) across the interface between the air and adhesive phases.

As for turbulence modelling, the RANS (Reynolds Averaged Navier Stokes) equations of the continuity, momentum and heat transfer are solved. A flow variable $\varphi(X,t)$ is split into two terms: a mean value $\bar{\varphi}$ and a fluctuating part $\varphi'$:

$$\varphi(X,t) = \bar{\varphi}(X,t) + \varphi'(X,t) \tag{9}$$

The turbulence models that are based on that Boussinesq hypothesis express the turbulent viscosity $\mu_t$ as a function of $k$, the turbulent kinetic energy and length scale $l$:

$$\mu_t = \rho l \sqrt{k} \tag{10}$$

where k is defined as:

$$k = \frac{1}{2}\overline{\underline{u}' \cdot \underline{u}'} \tag{11}$$

The k-ω SST model [22] is the turbulence model chosen, as it turns out to be more able to solve flows with strong adverse pressure gradient and flow separation, as it is the case of dual rectangular jets melt-blowing die flows [23]. A turbulence damping source term $S_{\omega,i}$ is introduced in the ω equation [24] to dampen the turbulence near the interface to avoid inaccurate results caused by non-physical velocity jumps.

$$S_{\omega,i} = A \Delta n \beta \rho_i \left(B \frac{6\mu_i}{\beta \rho_i \Delta n^2}\right)^2 \tag{12}$$

Where $A = 2.0\ \alpha_i |\nabla \alpha_i|$, $\alpha_i$ being the phase $i$ volume fraction, $\Delta n$ represents the grid size; $\beta = 0.075$ the destruction term; $\rho_i$ the density of the phase $i$; $\mu_i$ the viscosity of the phase $i$ and $B$ the damping factor. A damping factor of 10 has been selected, with the intention to not completely eliminate all the turbulence at the interface, but rather to capture the behaviour of the multiphase flow avoiding the introduction of numerical instability.

## 3. FLUID RHEOLOGY AND THERMOPHYSICAL PROPERTIES

The fibre fluid is modelled as a temperature-dependent non-Newtonian fluid. To capture the data of the measurements obtained from a parallel plate viscometer at different temperatures (Figure 1), the Cross-Arrhenius model is employed:

$$\mu_f = e^{\frac{E_a}{R}\left(\frac{1}{T} - \frac{1}{T_R}\right)} \frac{\mu_0}{1 + (\lambda \dot{\gamma})^N} \tag{13}$$

where $\mu_0$ is the zero shear viscosity, $\lambda$ the relaxation time, $\dot{\gamma}$ the shear rate and $N$ the power-law index. $\frac{E_a}{R}$ is the activation energy of the polymer divided by the ideal gas constant and $T_R$ is the reference temperature. For this fluid, $T_R = 150\ ºC = 423.15\ K$ and $\frac{E_a}{R} = 6843.83\ K$. The values of the cross law parameters are $\mu_0 = 2{,}4\ Pa.s$, $\lambda = 0.2\ ms$ and $N = 0.85$.

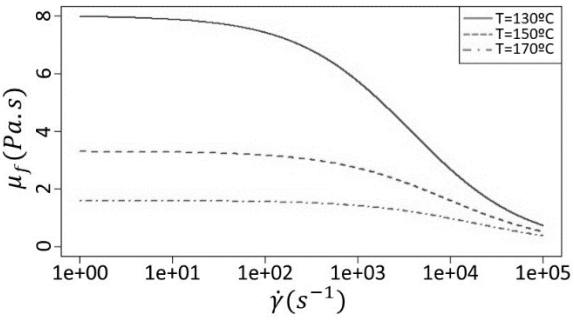


**Figure 1. Evolution of the dynamic viscosity $\mu_f$ as a function of the shear rate $\dot{\gamma}$ at different temperatures**

The air employed to attenuate the fibre follows the ideal gas law. The other thermophysical properties (specific heat, density, thermal conductivity, surface tension) are maintained constant for both the air and the fibre fluid.

## 4. FLOW DOMAIN AND DISCRETISATION

### *4.1. The boundary conditions and the flow domain mesh*

The flow domain is shown in Figure 2. The three entry ducts are the nozzle components. The central duct contains the fibre fluid, and the other ones air, with a hydraulic diameter of 0.52 mm.

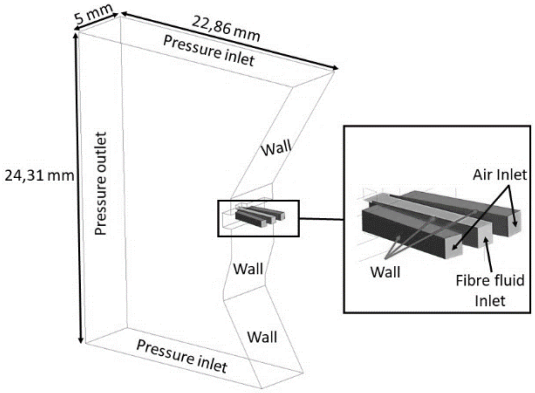


**Figure 2. The fluid flow domain boundary conditions with the three entry ducts**

The flow domain has been meshed by parametrising the number of division and node distribution at each edge. The structured mesh (Figure 3) is composed of 4 millions of hexahedral cells, with an average orthogonal quality of 0.99 and a mean aspect ratio of 7.29. To capture accurately volumetric fraction gradients at the interface between the air and the adhesive, an adaptive mesh refinement method is employed (see the cut view in Figure 3 for the interface where such method is employed). This approach allows for finer resolution without overly increasing the number of cells.

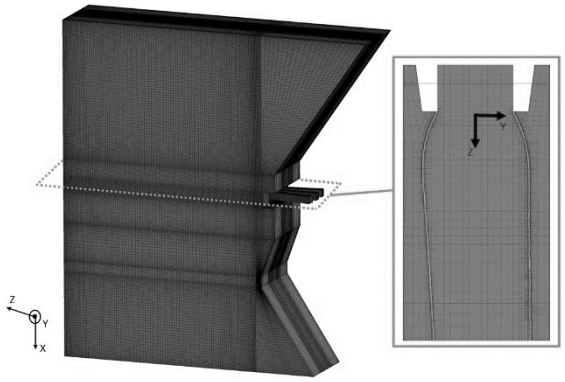

**Figure 3. The fluid flow domain mesh isometric view with the cut view showing the mesh interface refinement**

### *4.2. Spatial and temporal discretisation*

The governing equations of the flow are discretised using the finite volume method (FVM) and solved using Ansys® Fluent 2020 R1. Second-order accurate schemes are employed, and the PRESTO! (pressure staggering option) scheme is used for the discretisation of the pressure equation. The gradients are computed using the least squares cell based method and the discretised equations are solved in a coupled manner. As the explicit formulation is employed for the discretisation of the volume fraction equation, the first-order implicit method is used to perform the temporal discretisation.

### *4.3. Interface capturing method*

To capture the interface between the air and the adhesive, the compressive scheme [25] is employed. This scheme is based on a slope limiter that is used to handle sharp changes in the solution domain.

$$\alpha_{face} = \alpha_{donor} + \vartheta \nabla \alpha_{donor} \cdot \underline{dr} \qquad (14)$$

where $\alpha_{face}$ is the value of the volume fraction of the face; $\vartheta$ is the slope limiter value, $\alpha_{donor}$ is the value of the volume fraction of the donor cell and $\underline{dr}$ is the cell to face distance.

## 5. RESULTS AND DISCUSSION

In this section, the results obtained from the multiphase model, using the same configuration as in two experiments previously conducted by Formoso et al. [26], are presented. The experimental measurements for the two cases considered (EXP A3 and EXP A5) revealed different results in terms of fibre patterns and motion frequencies, as the combination of air-polymer flow rate ($m' = \frac{\dot{m}_a}{\dot{m}_f}$) is doubled from EXP A3 to EXP A5 while the temperature ratio ($T' = \frac{T_a - T_{amb}}{T_f - T_{amb}}$) is the same. The air-polymer flow rate ratio influence proved to be predominant over that of the temperature ratio,

therefore the study focuses on the effect of the air-polymer flow rate ratio. The frequencies of the fibre oscillations and the attenuation of the fibre are key results, which determine whether if the experiment is within the limits of the operating conditions window. Otherwise, instabilities can appear and are likely to generate defects on the final product. The experimental results indicate that in both cases, no fibre breakup has been observed. However, the range of fibre motion frequencies differs significantly between EXP A3 and EXP A5. To validate the results, the experimental measures are compared with the fibre attenuation of the CFD results as well as the fibre movement in both the YZ and ZX plane. The frequencies obtained from such movement are assessed by studying the temporal evolution of the minimum Y-coordinate of the fibre.

### *5.1. Grid convergence and time step size influence study*

A grid and time step size sensitivity analysis is performed by comparing three spatial resolutions and two temporal resolutions. The variations of the fibre diameter at two locations (Figure 4), as well as the total mass of fibre within the domain are analysed. A Richardson extrapolation is then conducted following the guidelines proposed by Celik [27]. The case considered for this study has an air-polymer flow rate $m' = 1.3$ and a temperature ratio $T' = 1.52$.

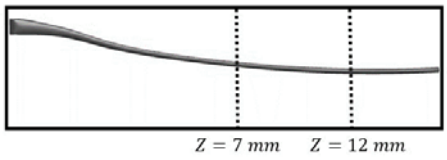


**Figure 4. The fibre in the ZX plane and the positions used to monitor the fibre dynamics**

The configurations of the three cases considered are presented in Table 1. The medium grid includes three levels of local refinement at the interface between the fibre and the surrounding air. This grid is compared against a coarser grid with two levels of refinement and a finer grid with four levels of refinement. For each grid, the simulation was run for the equivalent of two complete cycles of fibre dynamics (20.25 ms).

**Table 1. Grid characteristics**

| Grid | $\Delta t$ | Number of time steps simulated |
|---|---|---|
| Coarse (3,800,000 cells) | 2 μs | 10250 |
| Medium (4,600,000 cells) | 2 μs | 10250 |
| Fine (9,800,000 cells) | 1 μs | 20500 |

The grid convergence index (GCI) values obtained from the grid convergence test values (Table 2) proved to be accurate enough as the GCI values are all below 15% (Table 3).

**Table 2. Grid convergence test values**

| | **Coarse grid** | **Medium grid** | **Fine grid** |
|---|---|---|---|
| $\bar{D}_{Z=7\ mm}$ | 0.166±0.025 mm | 0.179±0.025 mm | 0.18±0.024 mm |
| $\bar{D}_{Z=12\ mm}$ | 0.124±0.027 mm | 0.135±0.025 mm | 0.139±0.026 mm |
| $\bar{M}_f$ | 1.454±0.03 mg | 1.491±0.025 mg | 1.492±0.025 mg |

**Table 3. Grid convergence index values**

| | $GCI_{Coarse}$ | $GCI_{Medium}$ | $GCI_{Fine}$ |
|---|---|---|---|
| $\bar{D}_{Z=7\ mm}$ | 9.84% | 0.76% | 0.058% |
| $\bar{D}_{Z=12\ mm}$ | 18.55% | 8.77% | 4.0% |
| $\bar{M}_f$ | 3.188% | 0.09% | 0.002% |

### *5.2. EXP A3 (m'=1.3; T'=1.52)*

As for EXP A3, the point at which the dynamics starts is located at Z=2 mm in both the YZ (Figure 5) and ZX (Figure 6) plane. The dynamics of the fibre in the YZ plane is stronger than in the ZX plane though, as wiggles can be noticed. Such dynamics is likely to create fibre patterns of a similar shape as those observed by Formoso et al. [26].

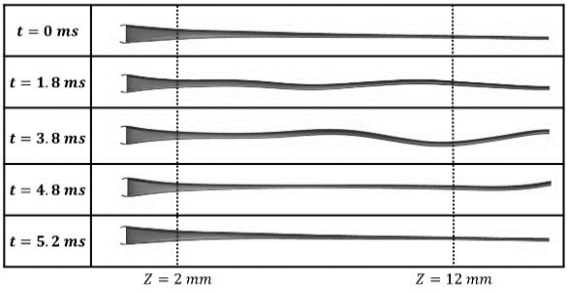


**Figure 5. EXP A3 fibre dynamics in the YZ plane**

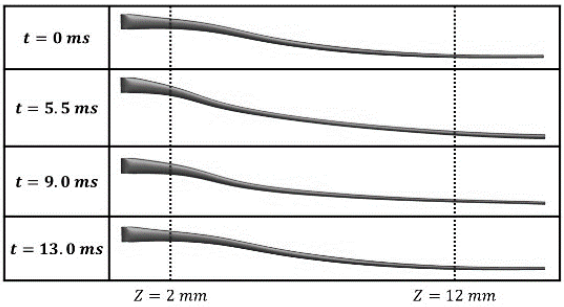


**Figure 6. EXP A3 fibre dynamics in the ZX plane**

The mean fibre attenuation obtained from the CFD model (Figure 7) is in agreement with the experimental results, as the differences between both results are within a 10% margin.

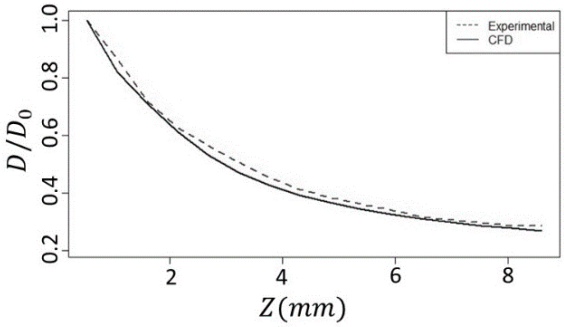


**Figure 7. Mean fibre attenuation comparison between experimental and CFD results for EXP A3**

The frequencies obtained from the variations in the minimum Y-coordinate of the fibre at $Z = 12\ mm$ (Figure 8) are consistent with the experimental data, displaying a range from 0.05 to 0.8 kHz, with the most significant peak being located between 0.175 and 0.23 kHz (Figure 9).

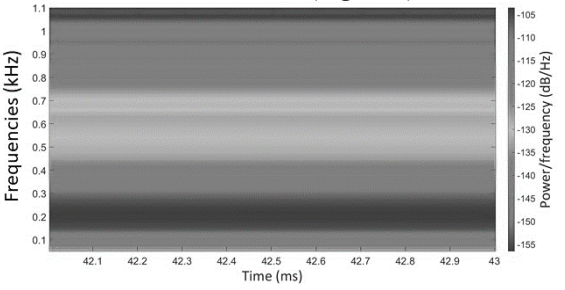


**Figure 8. Spectrogram depicting the variations of the minimum Y-coordinate of the fibre at Z=12 mm for EXP A3**

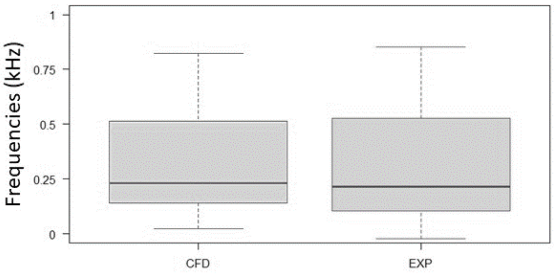


**Figure 9. Comparison between the frequencies obtained from experiments and CFD for EXP A3**

### *5.3. EXP A5 (m'=2.7; T'=1.52)*

As for EXP A5, where the dimensionless flow rate ratio is more than doubled that of EXP A3 by doubling the airflow rate $\dot{m}_a$, the fibre dynamics is significantly impacted. Hence, the fibre motion is predominantly two-dimensional, as the motion is mainly noticeable in the YZ plane.

Moreover, the amplitudes of the oscillations in the YZ plane are substantially steeper than in EXP A3 (Figure 10), with the highest amplitudes occurring near the starting point of the fibre oscillation (Z=2 mm).

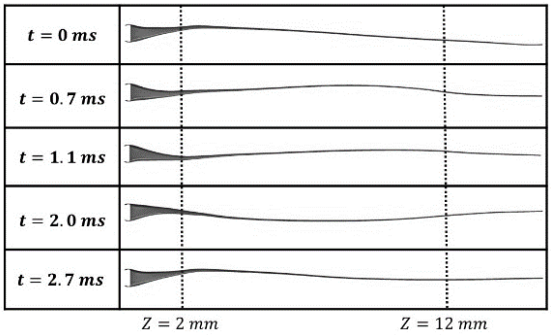


**Figure 10. EXP A5 fibre dynamics in the YZ plane**

The change in airflow rate also influences the mean fibre attenuation values (Figure 11), which are observed to be lower than those in EXP A3. The values obtained from the CFD model are still in agreement with the experimental ones.

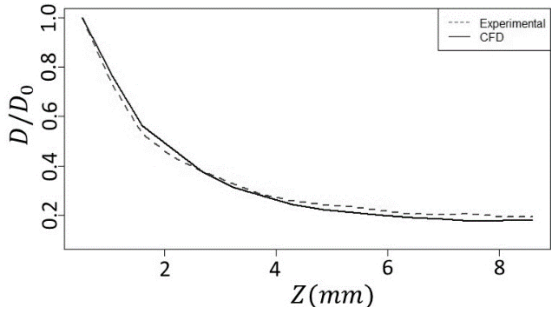


**Figure 11. Mean fibre attenuation comparison between experimental and CFD results for EXP A5**

As for the fibre motion, the frequency range obtained from simulations is considerably broader than in EXP A3. Indeed, the frequencies (Figure 12) extend from 0.1 to 1.7 kHz, with a high-frequency bandwidth ranging from 0.3 to 0.7 kHz and the most significant peak located between 0.45 and 0.5 kHz (Figure 13).

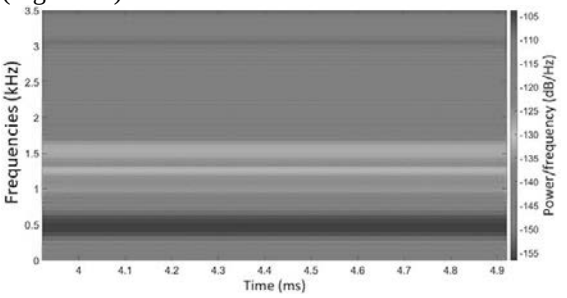


**Figure 12. Spectrogram depicting the variations of the minimum Y-coordinate of the fibre at Z=12 mm for EXP A5**

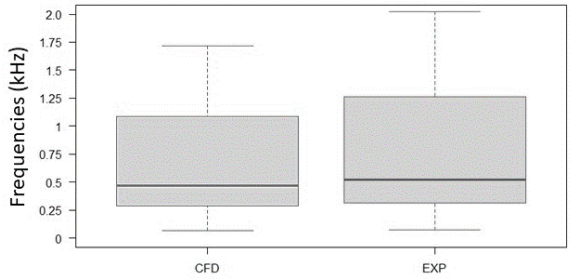


**Figure 13. Comparison between the frequencies obtained from experiments and CFD for EXP A5**

## 6. CONCLUSIONS

A mathematical multiphase model of the melt-blowing process in multi-hole nozzles was developed, by employing the VOF model. The fluid flow equations are discretised and solved using the finite volume method. The model provides information on the fibre dynamics as well as the air and temperature fields. The results showed that by doubling the air-polymer flow rate ratio, the attenuation of the fibre and the oscillations of the fibre motion are significantly affected. Furthermore, the agreement between the CFD results and experimental data of the fibre attenuation and dynamics provides confirmation that the adoption of the VOF model is appropriate and effective for studying the melt blowing process. This alignment between the numerical predictions and experimental observations validates the capability of this model to capture the complex phenomena occurring in the process not only qualitatively, but also quantitatively. This further establishes the suitability of multiphase simulations as a valuable tool for investigating and optimising the melt blowing process. By leveraging the capabilities of multiphase simulations, insights can be gained into the impact of the process parameters, and the performance of the melt blowing process can be predicted more efficiently and cost-effectively compared to relying solely on experimental trials.

## ACKNOWLEDGEMENTS

The authors gratefully acknowledge the financial support for this project from Ministerio de Ciencia e Innovación, Gobierno de España, RETOS-COLABORACION 2019 (grant number RTC2019007057-7).

## REFERENCES

[1] X. Hao and Y. Zeng, ‘A Review on the Studies of Air Flow Field and Fiber Formation Process during Melt Blowing’, *Ind. Eng. Chem. Res.*, vol. 58, no. 27, pp. 11624–11637, Jul. 2019, doi: 10.1021/acs.iecr.9b01694.

[2] Y. Kara and K. Molnár, ‘A review of processing strategies to generate melt-blown nano/microfiber mats for high-efficiency filtration applications’, *Journal of Industrial Textiles*, vol. 51, no. 1_suppl, pp. 137S-180S, Jun. 2022, doi: 10.1177/15280837211019488.

[3] P. Boggavarapu, S. P. Ramesh, M. M. Avulapati, and R. RV, ‘Secondary breakup of water and surrogate fuels: Breakup modes and resultant droplet sizes’, *International Journal of Multiphase Flow*, vol. 145, p. 103816, Dec. 2021, doi: 10.1016/J.IJMULTIPHASEFLOW.2021.103816.

[4] Y. Yang, Y. Zeng, Y. ; Yang, and Y. Zeng, ‘Measurement and Comparison of Melt-Blowing Airflow Fields: Nozzle Modifications to Reduce Turbulence and Fibre Whipping’, *Polymers 2021, Vol. 13, Page 719*, vol. 13, no. 5, p. 719, Feb. 2021, doi: 10.3390/POLYM13050719.

[5] S. Xie, G. Jiang, X. Wu, Y. Wang, H. Fang, and B. Shentu, ‘Air Recirculation and Its Effect on Microfiber Spinning in Blunt-Die Melt Blowing’, *Fibers and Polymers 2021 22:3*, vol. 22, no. 3, pp. 703–710, Mar. 2021, doi: 10.1007/S12221-021-0225-5.

[6] S. Kase and T. Matsuo, ‘Studies on melt spinning. I. Fundamental equations on the dynamics of melt spinning’, *Journal of Polymer Science Part A: General Papers*, vol. 3, no. 7, pp. 2541–2554, Jul. 1965, doi: 10.1002/pol.1965.100030712.

[7] B. Majumdar and R. L. Shambaugh, ‘Air drag on filaments in the melt blowing process’, *Journal of Rheology*, vol. 34, no. 4, pp. 591–601, May 1990, doi: 10.1122/1.550097.

[8] V. Bansal and R. L. Shambaugh, ‘On-line Determination of Diameter and Temperature during Melt Blowing of Polypropylene’, *Industrial & Engineering Chemistry Research*, vol. 37, no. 5, pp. 1799–1806, May 1998, doi: 10.1021/ie9709042.

[9] G. W. Sun, J. Song, L. Xu, and X. H. Wang, 'Numerical modelling of microfibers formation and motion during melt blowing', *https://doi.org/10.1080/00405000.2017.1342522*, vol. 109, no. 3, pp. 300–306, Mar. 2017, doi: 10.1080/00405000.2017.1342522.

[10] Kolev NI ,. Author and Lyczkowski RW ,. Reviewer, 'Multiphase Flow Dynamics, Volume 1: Fundamentals; Volume 2: Thermal and Mechanical Interactions', *Applied Mechanics Reviews*, vol. 56, no. 4, pp. B57–B59, Jul. 2003, doi: 10.1115/1.1579460.

[11] F. Denner, F. Evrard, and B. van Wachem, 'Breaching the capillary time-step constraint using a coupled VOF method with implicit surface tension', *Journal of Computational Physics*, vol. 459, p. 111128, Jun. 2022, doi: 10.1016/j.jcp.2022.111128.

[12] M. Vujanović, Z. Petranović, W. Edelbauer, and N. Duić, 'Modelling spray and combustion processes in diesel engine by using the coupled Eulerian–Eulerian and Eulerian–Lagrangian method', *Energy Conversion and Management*, vol. 125, pp. 15–25, Oct. 2016, doi: 10.1016/j.enconman.2016.03.072.

[13] Z. Petranović, W. Edelbauer, M. Vujanović, and N. Duić, 'Modelling of spray and combustion processes by using the Eulerian multiphase approach and detailed chemical kinetics', *Fuel*, vol. 191, pp. 25–35, Mar. 2017, doi: 10.1016/j.fuel.2016.11.051.

[14] N. C. Markatos, 'Modelling of two-phase transient flow and combustion of granular propellants', *International Journal of Multiphase Flow*, vol. 12, no. 6, pp. 913–933, Nov. 1986, doi: 10.1016/0301-9322(86)90035-2.

[15] D. B. Spalding, 'Numerical computation of multi-phase fluid flow and heat transfer', *In Von Karman Inst. for Fluid Dyn. Numerical Computation of Multi-Phase Flows*, pp. 161–191, 1981.

[16] G. V. Messa and S. and Malavasi, 'Numerical prediction of dispersed turbulent liquid–solid flows in vertical pipes', *Journal of Hydraulic Research*, vol. 52, no. 5, pp. 684–692, Sep. 2014, doi: 10.1080/00221686.2014.939110.

[17] Q. Xue *et al.*, 'An Eulerian CFD model and X-ray radiography for coupled nozzle flow and spray in internal combustion engines', *International Journal of Multiphase Flow*, vol. 70, pp. 77–88, Apr. 2015, doi: 10.1016/j.ijmultiphaseflow.2014.11.012.

[18] W. Edelbauer, 'Numerical simulation of cavitating injector flow and liquid spray break-up by combination of Eulerian–Eulerian and Volume-of-Fluid methods', *Computers & Fluids*, vol. 144, pp. 19–33, Feb. 2017, doi: 10.1016/j.compfluid.2016.11.019.

[19] T. Ménard, S. Tanguy, and A. Berlemont, 'Coupling level set/VOF/ghost fluid methods: Validation and application to 3D simulation of the primary break-up of a liquid jet', *International Journal of Multiphase Flow*, vol. 33, no. 5, pp. 510–524, May 2007, doi: 10.1016/j.ijmultiphaseflow.2006.11.001.

[20] B. Vila, D. Maza, and J. M. Pastor, 'A Three-Dimensional Multiphase Simulation of the Fiber Spiral Motion Under a Melt-Blowing Swirl Die', *Fibers Polym*, vol. 24, no. 7, pp. 2333–2341, Jul. 2023, doi: 10.1007/s12221-023-00228-2.

[21] J. U. Brackbill, D. B. Kothe, and C. Zemach, 'A continuum method for modeling surface tension', *Journal of Computational Physics*, vol. 100, no. 2, pp. 335–354, Jun. 1992, doi: 10.1016/0021-9991(92)90240-Y.

[22] F. R. Menter, 'Two-equation eddy-viscosity turbulence models for engineering applications', *AIAA Journal*, vol. 32, no. 8, pp. 1598–1605, Aug. 1994, doi: 10.2514/3.12149.

[23] Y. Wang and X. Wang, 'Numerical analysis of new modified melt-blowing dies for dual rectangular jets', *Polymer Engineering & Science*, vol. 54, no. 1, pp. 110–116, 2014, doi: 10.1002/pen.23536.

[24] Y. Egorov, M. Boucker, A. Martin, S. Pigny, M. Scheuerer, and S. Willemsen, 'Validation of CFD codes with PTS-relevant test cases', *5th Euratom Framework Programme ECORA project*, vol. 2004, pp. 91–116, 2004.

[25] G. Chen, Q. Wang, and S. He, 'Assessment of an Eulerian multi-fluid VOF model for simulation of multiphase flow in an industrial Ruhrstahl–Heraeus degasser', *Metall. Res. Technol.*, vol. 116, no. 6, Art. no. 6, 2019, doi: 10.1051/metal/2019049.

[26] I. Formoso *et al.*, 'Experimental study on the hot-melt adhesive pattern produced by melt blowing nozzle designs':, *https://doi.org/10.1177/1528083720978401*, Dec. 2020, doi: 10.1177/1528083720978401.

[27] I. Celik, 'Numerical Uncertainty in Fluid Flow Calculations: Needs for Future Research', *Journal of Fluids Engineering*, vol. 115, no. 2, pp. 194–195, Jun. 1993, doi: 10.1115/1.2910123.